CrystEngComm

Accepted Manuscript

ROYAL SOCIETY OF CHEMISTRY

www.rsc.org/crystengcomm

Hierarchical Multi-villous Nickel-cobalt Oxide Nanocyclobenzene Arrays: Morphology Control and Electrochemical Supercapacitive Behaviors

Jinbing Cheng[†a,b], Yang Lu[†a,c], Kangwen Qiu[†a.b], Deyang Zhang[†a,d], Chunlei Wang[a,b], Hailong Yan[a,b], Jinyou Xu[a,b], Yihe Zhang[d], Xianming Liu[e] and Yongsong Luo[*a,b]

[a] *School of Physics and Electronic Engineering, Xinyang Normal University, Xinyang 464000, P. R. China*

[b] *Key Laboratory of Advanced Micro/Nano Functional Materials, Xinyang Normal University, Xinyang 464000, P. R. China*

[c] *School of Material Science and Engineering, Hebei University of Technology, Tianjin 300130, P. R. China*

[d] *School of Materials Science and Technology, China University of Geosciences, Beijing 100083, P. R. China*

[e] *College of Chemistry and Chemical Engineering, Luoyang Normal University, Luoyang 471022, P. R. China*

Binary metal oxides have been regarded as ideal and potential anode materials, which can ameliorate and offset the electrochemical performance of single metal oxides, such as reversible capacity, structural stability and electronic conductivity. In this work, hierarchical multi-villous $NiCo_2O_4$ nanocyclobenzene arrays (NCAs) on nickel foam have been fabricated by a simple hydrothermal approach combined with a post-annealing treatment. Such unique array nanoarchitectures exhibit remarkable electrochemical performance with high capacitance and desirable cycle life at high rates. When evaluated as an electrode material for supercapacitors, the NCAs supported on nickel foam are able to deliver high specific capacitance of 1545 F g^{-1} at current densities of 5 A g^{-1} in 2 M KOH aqueous solution. In addition, the composite electrode shows excellent mechanical behavior and long-term cyclic stability (93.7% capacitance retention after 5000 cycles). All in all, the fabrication strategy presented

* To whom correspondence should be addressed： E-mail: ysluo@xynu.edu.cn

† These authors contribute equally to this work.

here is simple, cost-effective, and scalable, which opens new avenues for the large scale applications of these novel materials in energy storage.

Keywords: multi-villous, nanocyclobenzene, $NiCo_2O_4$, supercapacitors

1. Introduction

Over the past few years, the development of micro/nanoscales transition metal oxides with different morphologies have been noted to be one of the substantive challenges in materials science and technology considering their potential application in the fields of ion exchange,[1] catalysis processes,[2] and supercapacitors.[3] Supercapacitors, also widely known as electrochemical capacitors (ECs), have been considered as one of the most promising next generation energy-storage devices since they are able to offer higher power density with longer cycling lifespan than batteries, and store higher energy over conventional capacitors, which presently fill the gap between batteries and conventional capacitors.[4-8]

Regarding an intriguing supercapacitor, the superiority of electrode materials is crucial for the clean, efficient and versatile use of energy. It is worth noting that electrode materials play a vital role in the research of high-performance supercapacitors in terms of morphology, porosity, size, electronic conductivity, possible oxidation states, etc.[9,10] Especially, the research on flexible storage devices is increasingly important for the rapid development of portable electronic devices with lightweight and flexible designs. The key research of supercapacitors is the design of novel electrode materials with good specific capacitance and cycling stability and high power density. Although a variety of nanostructures have been created and tested to date, a great challenge is still represent to enhancing the capacity, maintaining the excellent rate capability and charge-discharge cycling life.[11,12] Metal oxides such as nickel cobaltite ($NiCo_2O_4$) has better conductivity and electrochemical activity than the single oxides due to the combined contributions from both nickel and cobalt ions in the oxide structures.[13] At present, $NiCo_2O_4$ with a various morphologies have been successfully fabricated, including three dimensional (3D) branch-like,[14] mono-disperse $NiCo_2O_4$ mesoporous micro-spheres,[15] 2D nanofilms,[16] mesoporous

nanoflakes,[17] nanosheets,[18-20] 1D nanoneedles,[21] nanowires,[22-24] and porous nanotubes.[25] Therefore $NiCo_2O_4$ has been conceived as a promising electrode material for supercapacitors (SCs) owing to its high specific capacitance, environmental compatibility and cost effectiveness.

In this paper, we report novel 3D hierarchical multi-villous $NiCo_2O_4$ nanocyclobenzene arrays on nickel foam by combining hydrothermal synthesis and annealing treatment. Based on this unique structure, these nanocyclobenzenes are intercrossed and interconnected with one another, forming an intricate transportation network to provide an excellent capability for fast ion and electron transfer. As a demonstration, we have investigated their electrochemical energy storage as electrodes in supercapacitors. As a consequence, these hierarchical multi-villous NCAs manifest ultrahigh capacitance and good cycling stability at high rates, even nice capacitance retention after 5000 cycles. These excellent results demonstrated that these unique $NiCo_2O_4$ arrays are promising candidates for electrochemical energy storage applications.

2. Experimental

Preparation of 3D hierarchical $NiCo_2O_4$ nanocyclobenzene arrays

All the reagents were analytical grade and directly used after purchase without further purification. Prior to deposition, nickel foam (1.5×4 cm in rectangular shape) were cleaned by sonication sequentially in acetone, 1 M HCl solution, deionized water, and ethanol for 15 min each, drying for standby. NCAs on nickel foam were synthesized via a simple one-pot hydrothermal process. 1 mmol (0.24 g) of $NiCl_2.6H_2O$ and 2 mmol (0.48 g) of $CoCl_2.6H_2O$ were dissolved into 35 mL of deionized water and 5 mL of ethanol absolute, followed by the addition of 15 mmol (0.90 g) of urea and 6 mmol (0.22 g) of NH_4F at room temperature , and the mixture was stirred to form a clear pink solution. Then the mixture was transferred into a 40 mL Teflon-lined stainless autoclave. Then, the well-cleaned nickel foam was immersed in the mixture, and the autoclave was kept at 120 ^oC for 4 h. After it was cooled down to room temperature, the product supported on the nickel foam was taken out and washed with

deionized water and ethanol several times and cleaned by ultrasonication to remove the loosely attached products on the surface. After that, the sample was dried at 70 ^{o}C for characterization. Finally, the as-prepared sample was annealed at 350 ^{o}C in air for 2 h , the temperature rising with a ramping rate of 1 ^{o}C min^{-1}.

Characterization

The crystalline structure and phase purity of the products were identified by X-ray diffraction (XRD) using a D8 Advance (Germany, Bruker) automated X-ray diffractometer system with Cu-Kα (λ = 1.5418 Å) radiation at 40 kV and 40 mA ranging from 10° to 80° at room temperature. Raman spectra were carried out using an INVIA Raman microprobe (Renishaw Instruments, England) with a 532 nm laser source and a 50×objective lens. Scanning electron microscopy (SEM) images were obtained using a HITACHI S-4800 microscope (Japan). The elemental analysis was carried out using a Bruker-QUANTAX, energy-dispersive X-ray spectroscope (EDS) attached to a FESEM. The Brunauer-Emmett-Teller (BET) surface area of the $NiCo_2O_4$ was determined through nitrogen sorption measurement at 77K conducted on Quadrasorb SI-MP Surface Area and Porosity Analyzer (American, Quantachrome). For the BET measurement, about 20 mg of the as-obtained sample powders were scratched from nickel foam.

Electrochemical evaluation

The electrochemical properties of NCAs were investigated with cyclic voltammetry (CV) and galvanostatic charge-discharge (CD) measurements in a conventional three-electrode cell employing a CHI 660E electrochemical workstation (Chenhua, Shanghai). The three-electrode cell contained a Pt foil served as the counter electrode, a standard calomel electrode (SCE) as the reference electrode and NCAs (about 3.3 mg cm^{-2}) grown on nickel foam as the working electrodes, with a solution of 2 M KOH as the electrolyte at room temperature. CV analysis was performed between 0 and 0.7 V *vs.* SCE at various scan rates ranging from 10 to 70 mV s^{-1}. Galvanostatic charge-discharge test was conducted in a stable potential window between 0 and 0.6 V

at different current densities of 1~20 A g^{-1}. Electrochemical impedance spectroscopy (EIS) measurements were performed by applying an alternate current (AC) voltage with 10 mV amplitude in a frequency range from 0.01 Hz to 100 kHz. The nominal area of the NCAs electrodes immersed into the electrolyte was controlled to be around 1.5 cm× 2 cm. The galvanostatic charge-discharge tests were conducted on a LAND battery program-control test system. The specific capacitance is calculated according to the following equation:

$$C = \frac{I\Delta t}{M\Delta V}$$

where C (F g^{-1}) is the specific capacitance, I (mA) represents the discharge current, and M (mg), ΔV (v) and Δt (s) designate the mass of active materials, potential drop during discharge and total discharge time, respectively.

3. Results and Discussions

Morphology and structural analysis

The crystallographic phase of the as-obtained NCAs products was studied by the XRD technique. Before XRD analysis, the NCAs powders were scratched from nickel foam in order to reduce the strong background signals of the nickel foam on the XRD peaks. The typical wide-angle diffraction patterns are shown in Fig. 1, which consists of seven well-defined diffraction peaks that can be well-indexed into a cubic spinel $NiCo_2O_4$ crystalline structure (JCPDF card No. 20-0781). In general, the coexistence of Co and Ni in the oxide should be in favor of the formation of $NiCo_2O_4$.[23] In order to further confirm the composition and structure of the $NiCo_2O_4$ samples, Raman analysis was performed. As shown in Fig. S1, four peaks at 187, 477.8, 523.5, and 671.2 cm^{-1} were observed. They are assigned to the F_{2g}, E_g, F_{2g}, and A_{1g} models of $NiCo_2O_4$, respectively. Therefore, only the Co-O and Ni-O vibrations of $NiCo_2O_4$ samples are detected but no signal from the OH group, indicating the cobalt and nickel metallic carbonate hydroxide salts are completely decomposed after calcinating at 350 ^oC. These results are consistent with those documented in previous reports.[26,27]

Fig. 2 gives the thermogravimetric and differential thermal analysis (TG-DTA) curves of the Ni-Co hydroxide precursor hydrothermal synthesized for 4 h in oxygen. It can be seen that the Ni-Co hydroxide begins to decompose at 220 ^{o}C. The curve change is mainly the evaporation of the water and other small molecules before 220 ^{o}C. In the DTA curve, there is a strong heat absorption peak at around 350 ^{o}C, which is originated from the decomposition of Ni-Co hydroxide to $NiCo_2O_4$. The result demonstrated that 350 ^{o}C is the reasonable annealing temperature for our route. Fig. 3 presents the design and synthesis strategy of the NCAs on Ni foam as a supercapacitor electrode. It can be seen that the whole process involves two steps: first, NCAs were evenly grown on the Ni foam via a facile modified hydrothermal process; second, the obtained NCAs were subsequent post-annealing in air atmosphere, the color of the NCAs changed and still well kept the benzene ring shape.

The scanning electron microscope (SEM) images of hierarchical multi-villous $NiCo_2O_4$ nanocyclobenzene arrays are shown in Fig. 4. As can be seen, the nanocyclobenzene arrays are uniformly grown on the skeleton of Ni foam to form a large-scale conformal coating (Fig. 4a). The higher magnification SEM images (Fig. 4b) show that the products are overlapping and intertwined in a clustered together, looking like a blooming flower. Fig. 4c,d exhibit cyclobenzene-like structure with the surface consisting of many villous-like nanowires (with a length of ~500 nm) and small circle shapes grown on the nanocyclobenzenes. Furthermore, the nanocyclobenzenes connect each other and grow aligned on the substrate. They are close to 7-9 μm. It is expected that these special structures would have large surface area and high capacitance due to the hierarchical arrays, which facilitate the access of electrolytes to activematerial of the electrode.

More detailed information about the morphological and structural features of the as-synthesized NCAs was studied by TEM, HRTEM and selected-area electron diffraction (SAED). Fig. 5a displays the whole view of the hierarchical multi-villous NCA structured arrays. It is clearly shown a hexagon profile and the nanocyclobenzenes are overlapping each other. A higher magnification image taken from a single nanocrystal within a nanocyclobenzene is depicted in Fig. 5b,

confirming that the nanoncyclobenzenes are of polycrystalline nature. Fig. 5c shows the HRTEM images recorded from the Fig. 5b. The clearly resolved lattice fringes were calculated to be about 0.472 nm, 0.247 nm and 0.205 nm, corresponding to the (111), (311) and (400) planes of spinel structured $NiCo_2O_4$. The SAED pattern (Fig. 5d) shows well-defined diffraction rings, indicating the crystalline nature of the cubic phase. These rings can be readily indexed to the (111), (220), (311), (400) and (422) planes of the cubic $NiCo_2O_4$ phase, which are consistent with the above XRD results.

In order to describe the porous characteristics and textural properties of the hierarchical NCAs more clearly, N_2 adsorption-desorption measurements were further performed. According to the IUPAC (International Union of Pure and Applied Chemistry) classifications of hysteresis loops,[28] Fig. 6 plots type IV isotherms with type H3 hysteresis loops, indicating the existence of a typical mesoporous microstructure.[29,30] The amount of nitrogen adsorbed increases rapidly at a relative pressure close to unity, which implies the existence of a large interconnection void or a void space within the nanocyclobenzenes. The pore-size-distribution (PSD) data (the inset in Fig. 6) shows that the size of the majority of the pores falls in the optimal range of 3-8 nm for the EC application. The mesoporous structure gives rise to a relatively high Brunauer-Emmett-Teller (BET) specific surface area of 120 m^2 g^{-1}. The high surface-area values and desired mesoporous nature of our samples satisfy the optimal performance requirements for supercapacitor applications.[31]

Effects of reaction time*:* The effects of reaction time were investigated. The growth process for the NCAs can be interpreted by inspecting the morphologies at different growth stages by controlling the time. After reacting for 2 h, the skeletons of nickel foam are decorated with thin nanoflakes (Fig. 7a,b). At the same time, the nanoflakes seem to be a bit disorganized and arranged disorderly. With increasing the reaction time to 6 h, the nanowires grow at the edge of the nanoflakes with a cross configuration at the base (Fig. 7c,d), finally producing the interesting nanoflake hetero-structured arrays (NFAs). The nanowires become longer and length up to around 2 μm. Clearly, no nanowires packed in the interspaces of the nanoflakes,

indicating that nanowires were preferentially deposited at the edge. Meanwhile, the length of nanowires could be easily controlled by the growth time.

Effects of concentration of NH_4F: In order to further study the morphology formation, we control the molar ratio of NH_4F during the growth (Fig. S2). It was apparent that, the nanostructures were prone to grow 1D nanopearl arrays (NPAs) without the addition of NH_4F (Fig. S2a,b). The nanowires arranged orderly and contained many granular pearls. When the molar weight of NH_4F increased to 12 mmol, the nanowires got so highly dense that the flake like framework looked slimy and agglomerate (Fig. S2c,d). NH_4F plays an important role in activating the substrates, resulting in the formation of this sort of morphology. After introducing NH_4F, the substrate may become activated to form an uneven layer which is apt to form interconnected flake-like structure. With flake growing up to a certain degree, there is a moderate amount of NH_4F on the surface of the flakes to promote thorn-like nanowires rooting in nanoflakes and stretching out to fill the intervals between the primary nanoflakes. The more contact with NH_4F, the more nanowires can be growed from nanoflakes. Futhermore, we also observe that NH_4F is associated with the adhesion between the substrate and the arrays. For nickel cobalt precursor arrays with 12 mmol of NH_4F, an average mass loading of 2.5 mg cm^{-2} is achieved even after 2.5 h of ultrasonication. Without NH_4F, the nanowire film can be removed easily by several minutes of ultrasonication and less than 1 mg cm^{-2} of active material is retained. The results may be attributed to the presence of F^-, which can stimulate the substrates to produce more active sites for nucleation.

Moreover, the different morphologies of $NiCo_2O_4$ nanostructures are also shown in Fig. S3. As can be seen, the $NiCo_2O_4$ nanostructures are highly consistent grown on Ni foam (Fig. S3a-c). At the same time, the corresponding results of EDS microanalysis are shown in Fig. S3d-f. It is found that the nanostructures consists of O, Co, and Ni elements, and the atomic ratio of cobalt to nickel is approximately 2:1.

Electrochemical measurement

Potential sweep cyclic voltammetric (CV) measurements were usually performed in a potential range to examine the electrochemical characteristics and quantify the specific capacitance of as-prepared electrode. Fig. 8a shows CV comparison of the $NiCo_2O_4$ nanocyclobenzene arrays, the $NiCo_2O_4$ nanoflake arrays with the react time of 6 h and the $NiCo_2O_4$ nanopearl arrays obtained without adding NH_4F at a scan rate of 40 mV s^{-1}. Obviously, the NCAs show a higher current density and CV curve area than the NFAs and NPAs, indicating the hierarchical NCAs architecture has a higher electrochemical reaction activity. It is noteworthy that variations in redox peak positions can be observed from the three samples. This may be ascribed to the difference in electrode polarization behavior during the CV tests. As depicted, the polarization behavior is closely related to the chemical composition and physical morphology of the electrode material. The redox reactions in the alkaline electrolyte are expressed as follows:[32-35]

$$NiCo_2O_4 + OH^- + H_2O \longleftrightarrow NiOOH + 2CoOOH + 2e^- \quad (1)$$

$$CoOOH + OH^- \longleftrightarrow CoO_2 + H_2O + e^- \quad (2)$$

Fig. 8b shows the typical CV curves of the NCAs with different scan rates of 10-70 mV s^{-1}. The shape of the CV curves demonstrates the pseudocapacitive characteristics of the NCAs electrode. Generally two pairs of broadly and poorly defined redox peaks are observed in the CV plots, which originating from the faradaic redox reactions related to M-O/M-O-OH, where M represents both the Ni and Co ions.[1,8,36-38] With the increasing of scan rate, the current subsequently enhanced while the shape of the CV curves mainly retains unchanged except for the small shift of the peak position, thus revealing the prominent electrochemical reversibility and apparent high-rate performance.

Based on the above results, NCAs exhibit higher specific capacitance and more excellent cycle stability, we further investigated the galvanostatic charge-discharge (GCD) behavior of at different current density at potentials between 0 and 0.6 V. The

corresponding results are shown in Fig. 8c. The voltage plateaus at around 0.4 V in the GCD curves indicate the existence of faradaic processes, which is consistent with the CV curves. With the increasing of current density, the GCD curves still hold excellent symmetry, without obvious IR drop, indicating the outstanding electrochemical reversibility. Fig. 8d gives the relationship between the specific capacitance or capacity retention and current density, exposing very high specific capacitance and good rate capability. At a relatively low current density of 5 A g^{-1}, the NCA sample delivers a high capacitance of 1545 F g^{-1}, even when the current density is 20 A g^{-1}, the capacitance can still remain at 1166 F g^{-1} (~75.5 % retention). The NCA has a higher specific capacitance than the $NiCo_2O_4$ nanowire (401 F g^{-1})[39] and $NiCo_2O_4$ nanourchin (658 F g^{-1})[40].

The cycle stability of supercapacitors is a crucial parameter for practical applications. The long-term stability of the electrodes is examined at 15 A g^{-1} as shown in Fig. 9a. It is found that the NCAs electrode capacitance retention about is more than 93% of initial value after 5000 cycles and they show a greater capacitance retention than the $NiCo_2O_4$ nanowires (90%)[39] . Fig. 9b shows the specific capacitance of the different electrode materials with the same current density. The specific capacitance of NCAs is much higher than the NFAs and NPAs, which is consistent with the results of the CV tests. These results can be attributed to the 3D mesoporous netstructure and the more active substances of NCAs under the same condition. In this work, compared with the NPAs and NFAs, the NCAs electrode shows a smaller resistance, as exhibited in Fig. 9c. The interconnection network of NCAs directly grown on nickel foam guarantees good mechanical adhesion and intrinsic electrical conductivity to the underneath current collector,[41] thus builds up an express path for fast electron transport, and avoids the use of conductive additive and polymer binder which usually add extra interfacial resistance. Ultrathin nanocyclobenzenes cross together, they support each other, leading to the unique structure stability. Such a firm and interconnecting framework is full able to stand against the structure damage caused by volume expansion during cycling process, resulting in an enhanced stability. As shown in Fig. 9d, the tailored porous NCAs

facilitate the penetration and diffusion of ions and electrons.

4. Conclusions

In summary, hierarchical multi-villous $NiCo_2O_4$ arrays on Ni foam have been successfully synthesized via a facile hydrothermal method combined a subsequent calcination treatment. We have established a template-free strategy to fabricate ultralayered mesoporous nickel cobaltite oxide, which is constructed from quasi-single-crystalline $NiCo_2O_4$ nanocyclobenzene building blocks. The unique 3D NCAs are demonstrated to be an interesting electroactive material for ECs, with large capacitance, high rate capability, and excellent cycle stability. We also show that the coexistence of nickel and cobalt ions, mesoporous characteristics, and ultralayered structure are important for the high electrochemical performance of the ultralayered mesoporous NCAs electrode. The novel NCAs electrode delivered a desirable specific capacitance of 1545 F g^{-1} at 5 A g^{-1}, and even 1166 F g^{-1} at 20 A g^{-1}. In addition, the specific capacitance degradation of ca. 7% after 5000 continuous cycles at a current density of 15 A g^{-1} indicated the good electrochemical stability of the ultralayered mesoporous NCAs electrode at high rates. More importantly, the preparation strategy we described here is simple and cost-effective enough for even large-scale production of the NCAs with good electrochemical performance for ECs, and even for lithium ion battery application. In this context, these $NiCo_2O_4$ nanostructures possess a great promise for the application as supercapacitor electrode.

Acknowledgments

This work was financially supported by the National Natural Science Foundation of China (Nos. U1304108 and U1204501), the Innovative Research Team (in Science and Technology) in University of Henan Province (Nos. 13IRTSTHN018). The authors are indebted to Dr D. L. Xu for their technical assistances and kind help.

References

1 Z. Z. Lin, F. L. Jiang, L. Chen, C. Y. Yue, D. Q. Yuan, A. J. Lan and M. C. Hong,

Cryst.Growth Des., 2007, **7**, 1712.

2 Y. Wan and D. Y. Zhao, *Chem. Rev*., 2007, **107**, 2822.

3 S. L. Xiong, C. Z. Yuan, X. G. Zhang, B. J. Xi and Y. T. Qian, *Chem. Eur. J*., 2009, **15**, 5320.

4 P. Simon and Y. Gogotsi, *Nat. Mater*., 2008, **7**, 845.

5 C. H. An, Y. J. Wang, Y. N. Huang, Y. N. Xu, C. C. Xu, L. F. Jiao and H. T. Yuan, *CrystEngComm*, 2014, **16**, 385.

6 C. Zhou, Y. W. Zhang, Y. Y. Li and J. P. Liu, *Nano lett*., 2013, **13**, 2078.

7 H. J. Yan, J. W. Bai, J. Wang, X. Y. Zhang, B. Wang, Q. Liu and L. H. Liu, *CrystEngComm*, 2013, **15**, 10007.

8 L. Q. Mai, F. Yang, Y. L. Zhao, X. Xu, L. Xu and Y. Z. Luo, *Nat. Commun*., 2011, **2**, 381.

9 H. Jiang, J. Ma and C. Z. Li, *Chem. Commun*., 2012, **48**, 4465.

10 T. Y. Wei, C. H. Chen, H. C. Chien, S. Y. Lu and C. C. Hu, *Adv. Mater*., 2010, **22**, 347.

11 J. T. Zhang and C. M. Li, *Chem. Soc. Rev*., 2012, **41**, 7016.

12 L. Yang, S. Cheng, Y. Ding, X. Zhu, Z. L.Wang and M. L. Liu, *Nano lett*., 2011, **12**, 321.

13 R. R. Salunkhe, K. Jang, H. Yu, S. Yu, T. Ganesh, S. H. Han and H. Ahn, *J. Alloys Compd*., 2011, **509**, 6677.

14 R. P. Silva, S. Eugenio, T. M. Silva, M. J. Carmezim, and M. F. Montemor, *J. Phys. Chem. C*, 2012, **116**, 22425.

15 J. F. Li, S. L. Xiong, Y. R. Liu, Z. C. Ju and Y. T. Qian, *ACS Appl. Mater. Interfaces*, 2013, **5**, 981.

16 L. F. Hu, L. M. Wu, M. Y. Liao and X. S. Fang, *Adv. Mater*., 2011, **23**, 1988.

17 L. X. Zhang, S. L. Zhang, K. J. Zhang, G. J. Xu, X. He, S. M. Dong, Z. H. Liu, C. S. Huang and G. L. Cui, *Chem. Comm*., 2013, **49**, 3540.

18 X. H. Lu, X. Huang, S. L. Xie, T. Zhai, C. S. Wang, P. Zhang, M. H. Yu, W. Li, C. L. Liang and Y. X. Tong, *J. Mater. Chem*., 2012, **22**, 13357.

19 C. Z. Yuan, J. Y. Li, L. R. Hou, X. G. Zhang, L. F. Shen and X. W. Lou, *Adv. Funct.*

Mater., 2012, **22**, 4592.

20 G. Q. Zhang and X. W. Lou, *Sci. Rep.*, 2013, **3**, 1470.

21 G. Q. Zhang, H. B. Wu, H. E. Hoster, M. B.C. Park and X. W. Lou, *Energy Environ. Sci*., 2012, **5**, 9453.

22 Q. F. Wang, X. F. Wang, B. Liu, G. Yu, X. J. Hou, D. Chen and G. Z. Shen, *J. Mater. Chem. A*., 2013, **1**, 2468.

23 H. L. Wang, Q. M. Gao and L. Jiang, *Small*, 2011, **7**, 2454.

24 H. Jiang, J. Ma and C. Z. Li, *Chem. Comm*., 2012, **48**, 4465.

25 L. L. Li, S. J. Peng, Y. L. Cheah, P. F. Teh, J. Wang, G. Wee, Y. W. Ko, C. L. Wong and M. Srinivasan, *Chem. Eur. J*., 2013, **19**, 5892.

26 Z. A. Hu, Y. L. Xie, Y. X. Wang, L. J. Xie, G. R. Fu, X. Q. Jin, Z. Y. Zhang, Y. Y. Yang and H. Y. Wu, *J. Phys. Chem. C*., 2009, **113**, 12502.

27 J. H. Zhong, Z. L. Wang, G. R. Li, J. W. Wang, Y. N. Ou and Y. X. Tong, *J. Mater. Chem*., 2012, **22**, 5656.

28 W. Xiong, M. X. Liu, L. H. Gan, Y. K. Lv, Y. Li, L. Yang, Z. J. Xu, Z. X. Hao, H. L. Liu and L. W. Chen, *J. Power Sources*, 2011, **196**, 10461.

29 D. Grosso, G. Illia, E. L. Crepaldi, B. Charleux and C. Sanchez, *Adv. Funct. Mater*., 2003, **13**, 37.

30 W. Y. Li, K. B. Xu, G. S. Song, X. Y. Zhou, R. J. Zou, J. M. Yang, Z. G. Chen and J. Q. Hu, *CrystEngComm*, 2014, **16**, 2335.

31 M. Huang, F. Li, J. Y. Ji, Y. X. Zhang, X. L. Zhao and X. Gao, *CrystEngComm*, 2014, **16**, 2878.

32 X. Wang, X. D. Han, M. F. Lim, N. Singh, C. L. Gan, J. Ma and P. S. Lee, *J. Phys. Chem. C*, 2012, **116**, 12448.

33 V. Gupta, S. Gupta and N. Miura, *J. Power Source*, 2008, **175**, 680.

34 C. C. Hu and C. Y. Cheng, *J. Electrochem. Solid-State Lett*., 2002, **5**, A43.

35 G. X. Hu, C. H. Tang, C. X. Li, H. M. Li, Y. Wang and H. Gong, *J. Electrochem. Soc*., 2011, **158**, A695.

36 T. Wu, J. Y. Li, L. R. Hou, C. Z. Yuan, L. Yang and X. G. Zhang, *Electrochim. Acta*, 2012, **81**, 172.

37 H. W. Wang, Z. A. Hu, Y. Q. Chang, Y. L. Chen, H. Y. Wu, Z. Y. Zhang and Y. Y. Yang, *J. Mater. Chem*., 2011, **21**, 10504.

38 M. Hamdani, R. N. Singh and P. Chartier, *Int. J. Electrochem. Sci*., 2010, **5**, 556.

39 C. Z. Yuan, J. Y. Li, L. R. Hong, L. Yang, L. F. Shen and X. G. Zhang, *J. Mater. Chem*., 2012, **22**, 16084.

40 J. W. Xiao and S. H. Yang, *RSC Adv*., 2011, **1**, 588.

41 T. Yu, Y. W. Zhu, X. J. Xu, P. Chen, C. T. Lim, J. T. L. Thong and C. H. Sow, *Adv. Mater*., 2005, **17**, 1595.

Figure captions

Fig. 1 XRD pattern of the $NiCo_2O_4$ nanocyclobenzene arrays.

Fig. 2 TG and DTA curves for the precursor after hydrothermal synthesis for 4 h.

Fig. 3 Schematic illustration for the formation processes of the $NiCo_2O_4$ nanocyclobenzene.

Fig. 4 (a-d) Typical SEM images of $NiCo_2O_4$ arrays on Ni foam at different magnifications.

Fig. 5 (a, b) Low-magnification and high-magnification TEM images of the NCAs;

(c) the HRTEM image of (b); (d) the corresponding SAED patterns from NCAs.

Fig. 6 Nitrogen adsorption and desorption isotherms measured at 77 K for the NCAs, and (the inset) Corresponding Barrett-Joyner-Halenda (BJH) pore size distribution curves.

Fig. 7 SEM images of the precursor obtained with the assistance of 6 mmol NH_4F at various reaction stages by setting the reaction time to (a, b) 2 h; (c, d) 6 h.

Fig. 8 Electrochemical characterization of supercapacitors: (a) CV curves of the $NiCo_2O_4$ nanocyclobenzene arrays, the $NiCo_2O_4$ nanoflake arrays obtained by reaction of 6 h and the $NiCo_2O_4$ nanopearl arrays obtained without adding the NH_4F; (b) CV curves at different scan rates of NCAs sample; (c) Galvanostatic charge-discharge curves of NCAs sample at various current densities; (d) specific capacitance and capacity retention as a function of current density.

Fig. 9 (a) Cycling performance of the NCAs, NFAs and NPAs electrodes at a current density of 15 A g^{-1}; (b) The comparison of specific capacitance at various current densities; (c) Electrochemical impedance spectra (EIS) obtained from the NPAs to NCAs electrodes; The inset shows the enlarged EIS of the electrodes; (d) Schematic diagram showing the kinetic advantages of the hybrid arrays in electrochemical energy storage.

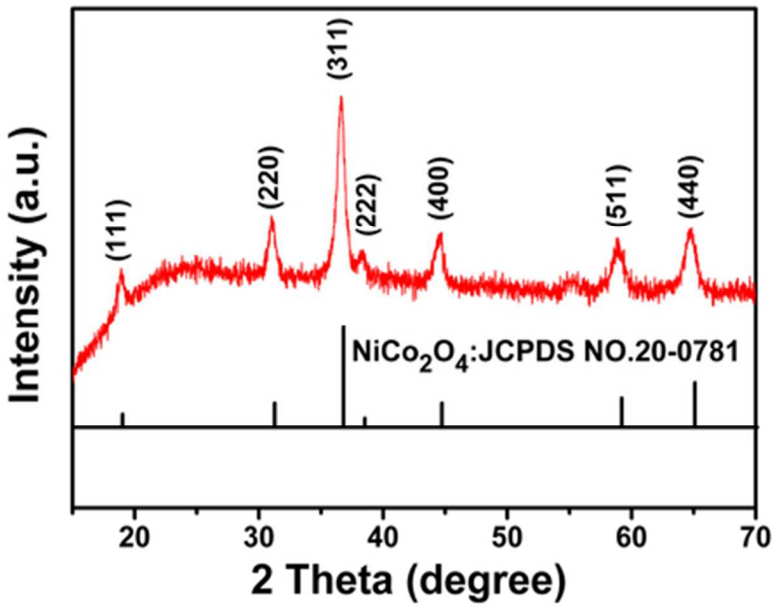

48x33mm (300 x 300 DPI)

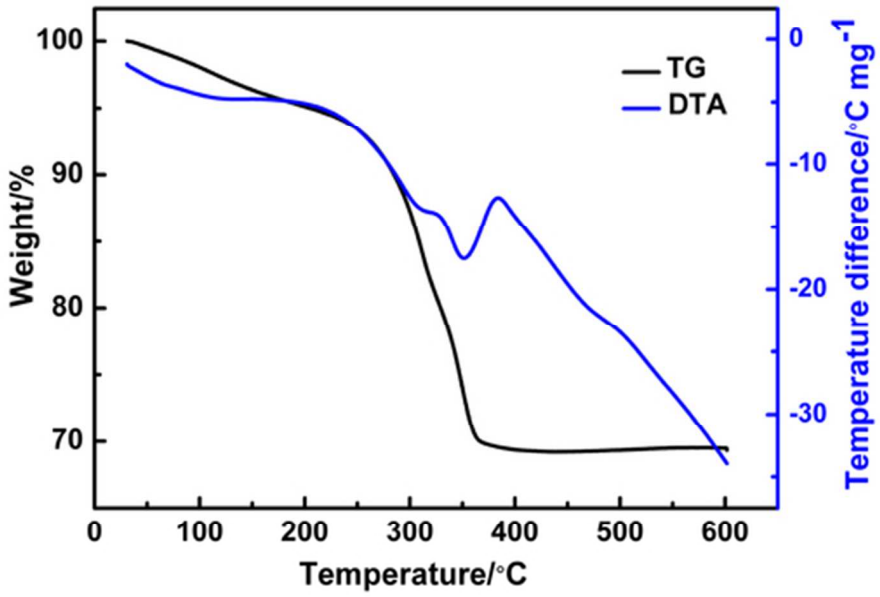

48x33mm (300 x 300 DPI)

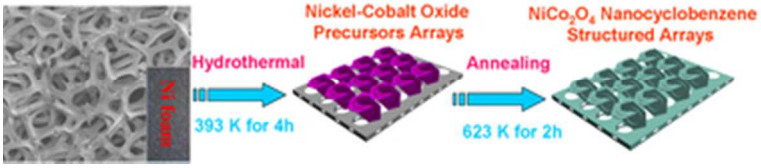

32x6mm (300 x 300 DPI)

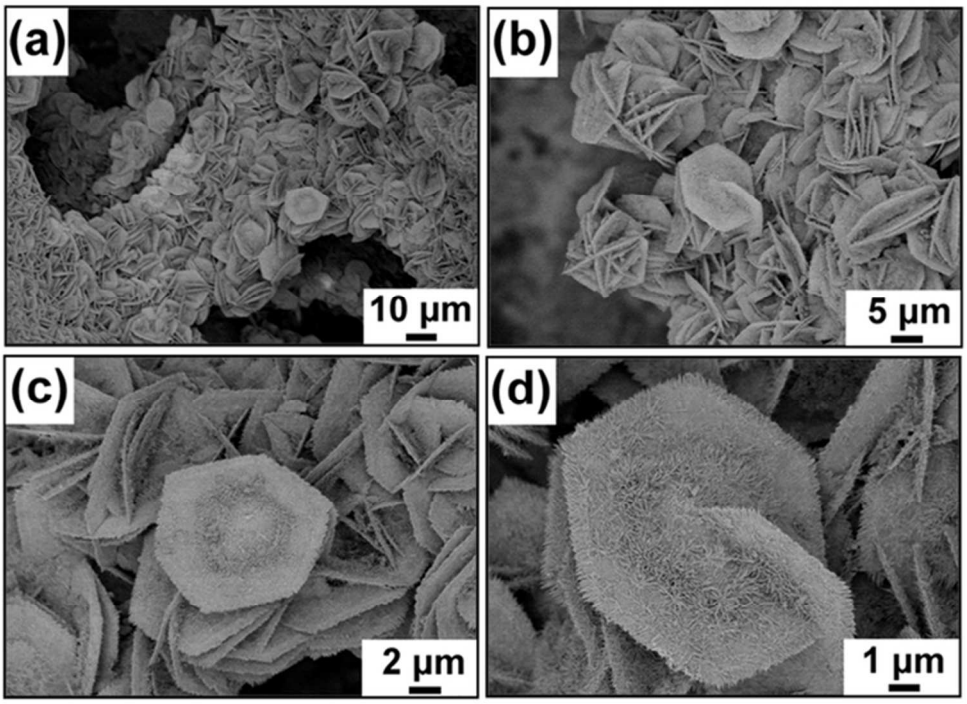

59x42mm (300 x 300 DPI)

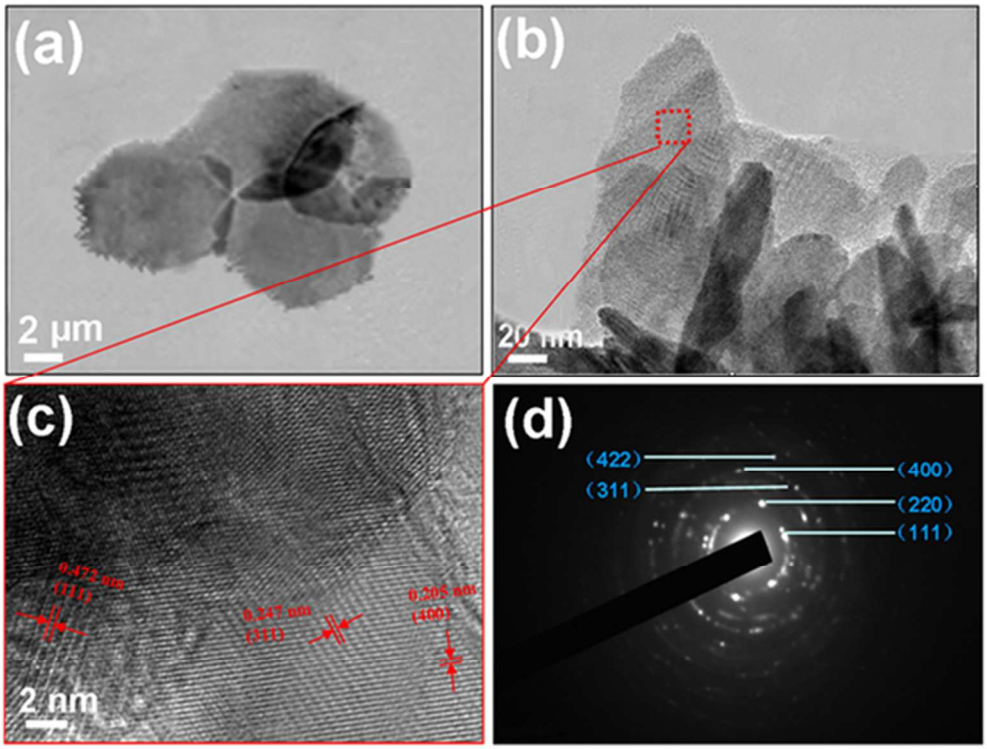

52x39mm (300 x 300 DPI)

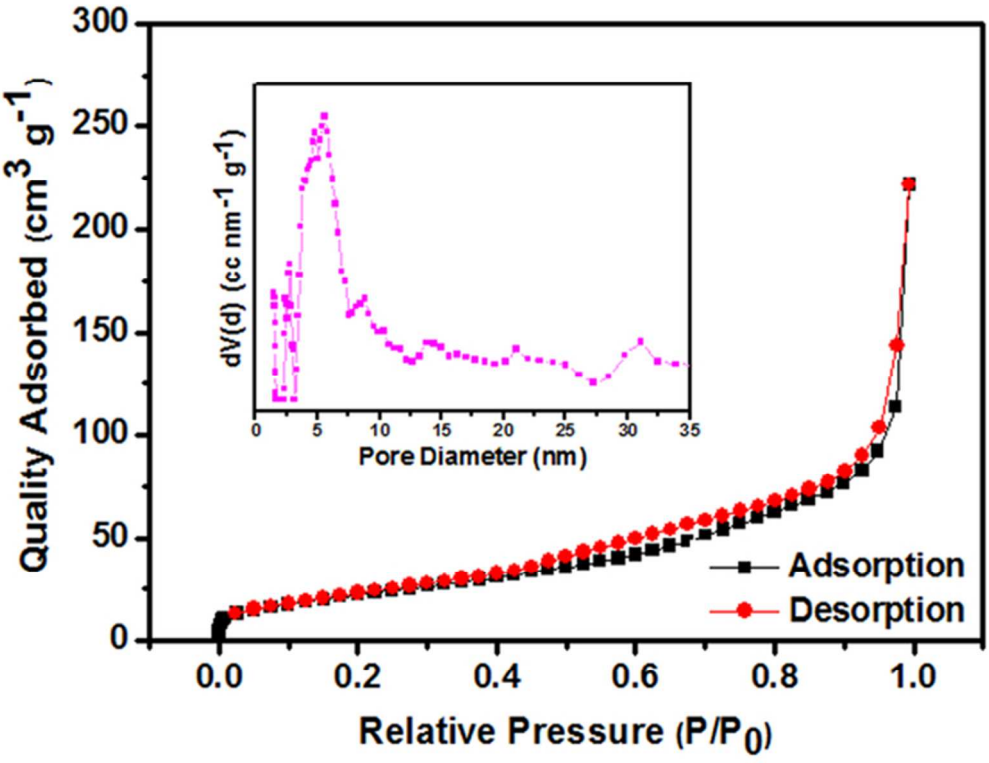

54x42mm (300 x 300 DPI)

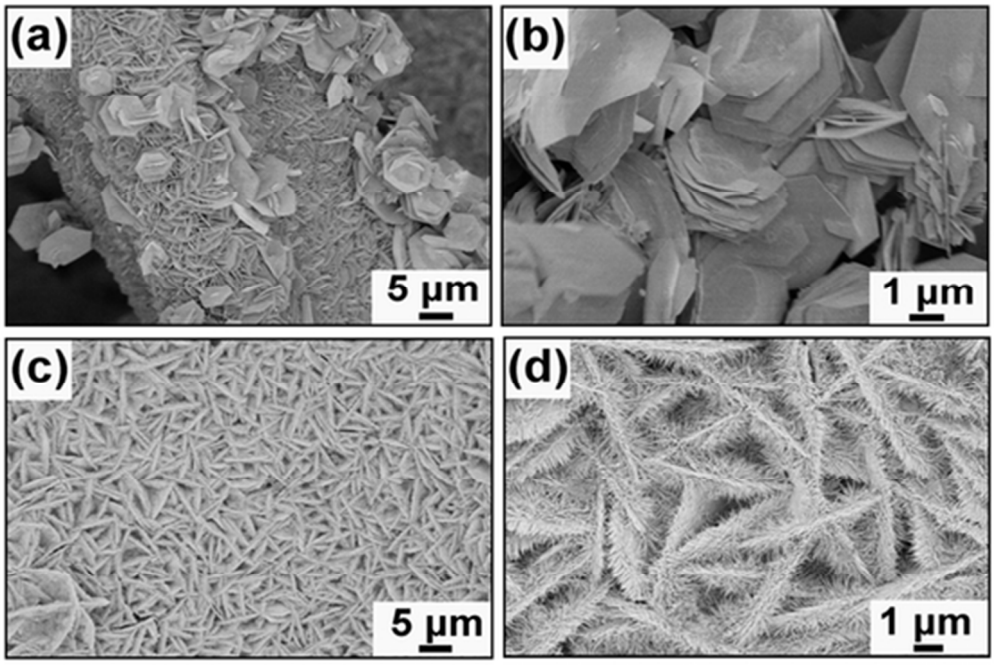

46x31mm (300 x 300 DPI)

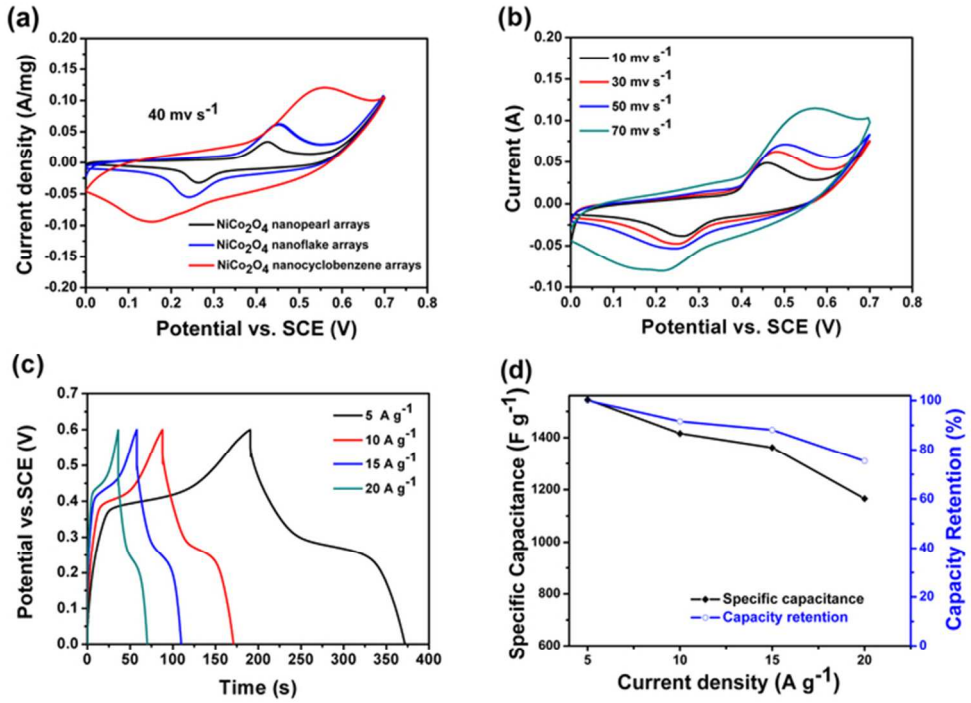

63x49mm (300 x 300 DPI)

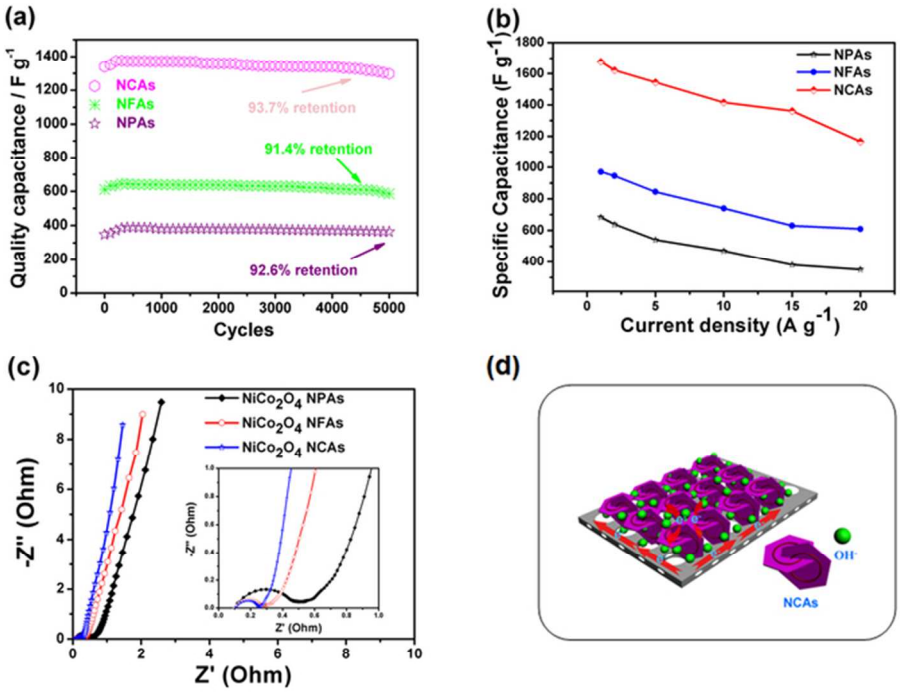

63x49mm (300 x 300 DPI)